MNRAS 000, 1–15 (2021) Preprint 15 February 2022 Compiled using MNRAS LATEX style file v3.0

The X-ray spectral-timing contribution of the stellar wind in the hard state of Cyg X-1

E. V. Lai,[1]★ B. De Marco[1,2], A. A. Zdziarski[1], T. M. Belloni[3], S. Mondal[1,3], P. Uttley[4], V. Grinberg[5], J. Wilms[6], A. Różańska[1]

[1]*Nicolaus Copernicus Astronomical Center, PAN, ul. Bartycka 18, Warsaw 00-716 Poland*
[2]*Departament de Física, EEBE, Universitat Politècnica de Catalunya, Av. Eduard Maristany, 16, Barcelona 08019, Spain*
[3]*INAF - Osservatorio Astronomico di Brera Via E. Bianchi 46, I-23807 Merate, Italy*
[4]*Anton Pannekoek Institute, University of Amsterdam, Science Park 904, 1098 XH Amsterdam, The Netherlands*
[5]*European Space Agency (ESA), European Space Research and Technology Centre (ESTEC), Keplerlaan 1, 2201 AZ Noordwijk, the Netherlands*
[6]*Dr. Karl Remeis-Observatory, University of Erlangen-Nuremberg, Sternwartstr. 7, 96049 Bamberg, Germany*

Accepted XXX. Received YYY; in original form ZZZ

ABSTRACT

The clumpy stellar wind from the companion star in high mass X-ray binaries causes variable, partial absorption of the emission from the X-ray source. We studied XMM-Newton observations from the 7.22 d–long "Cyg X-1 Hard state Observations of a Complete Binary Orbit in X-rays" (CHOCBOX) monitoring campaign, in order to constrain the effects of the stellar wind on the short-timescale X-ray spectral-timing properties of the source. We find these properties to change significantly in the presence of the wind. In particular, the longest sampled timescales (corresponding to temporal frequencies of $\nu \sim 0.1$–1 Hz) reveal an enhancement of the fractional variability power, while on the shortest sampled timescales ($\nu \sim 1$–10 Hz) the variability is suppressed. In addition, we observe a reduction (by up to a factor of ~ 1.8) of the otherwise high coherence between soft and hard band light curves, as well as of the amplitude of the hard X-ray lags intrinsic to the X-ray continuum. The observed increase of low frequency variability power can be explained in terms of variations of the wind column density as a consequence of motions of the intervening clumps. In this scenario (and assuming a terminal velocity of $v_\infty = 2400$ km s^{-1}), we obtain an estimate of $l \sim 0.5$–$1.5 \times 10^{-4} R_*$ for the average radial size of a clump. On the other hand, we suggest the behaviour at high frequencies to be due to scattering in an optically thicker medium, possibly formed by collision of the stellar wind with the edge of the disc.

Key words: X-rays: binaries; black hole physics; X-rays: individual (Cyg X-1); stars: wind, outflows;

1 INTRODUCTION

Black hole X-ray binaries (BHXRBs) are observed to occasionally and recursively undergo dramatic changes of their X-ray spectral and timing properties (e.g. Homan & Belloni 2005; Belloni 2010; Belloni et al. 2011). This behaviour is commonly ascribed to changes in the inner structure of the accretion flow (e.g. Gilfanov 2010), and associated with hysteresis between two main accretion states, the so-called soft and hard states (e.g. Zdziarski & Gierliński 2004). During the soft state most of the observed X-ray emission is consistent with being produced in a geometrically thin and optically thick disc (Shakura & Sunyaev 1973), and is characterized by a low level of rapid (from tens of seconds to milliseconds) X-ray variability (root mean square, rms, amplitude less than ~ 5 percent, e.g. Muñoz-Darias et al. 2011). In the hard state the X-ray spectrum is dominated by Comptonised emission. This is due to scattering of thermal photons from the optically thick disc (e.g. Shapiro et al. 1976; Ichimaru 1977; Sunyaev & Truemper 1979; Narayan & Yi 1994) and/or of synchrotron photons from the inner hot flow (Vurm & Poutanen 2008; Veledina et al. 2011) in a cloud of hot electrons, commonly referred to as hot corona, located close to the black hole (BH). This state is characterized by high levels of rapid X-ray variability (rms even exceeding 30 percent, Muñoz-Darias et al. 2011) and a complex distribution over frequency of the X-ray variability power (e.g. Belloni et al. 2005). While the phenomenology of these states is well established, the physical origin is still largely debated.

Cygnus X-1 (hereafter Cyg X-1) is amongst the best studied X-ray binary systems. It is composed of a BH with $M_\odot = 21.2 \pm 2.2\,\mathrm{M}_\odot$ and its supergiant O9.7 Iab companion star (HDE 226868) with $M_* = 40.6^{+7.7}_{-7.1}\,\mathrm{M}_\odot$ and $R_* = 22.3 \pm 1.8\,\mathrm{R}_\odot$ (Miller-Jones et al.

★ E-mail: eleonorav@camk.edu.pl

2021). The system is characterised by a quasi-circular orbit with an orbital period of 5.599829(16) d (Gies et al. 2003). Due to the size of the companion, this system is classified as a high mass X-ray binary, where the BH accretes mass via the strong stellar wind of the supergiant.

Like all other BHXRBs, Cyg X-1 shows complex temporal frequency dependence of its X-ray variability power, with a power spectral density function (PSD) characterized by two main broad "humps" in the hard state, that change drastically to a smoother profile in the soft state (e.g. Nowak et al. 1999; Pottschmidt et al. 2000, 2003; Axelsson et al. 2005; Böck et al. 2011; Grinberg et al. 2014). In addition, highly coherent hard ($E \gtrsim 1$ keV) and soft ($E \lesssim 1$ keV) X-ray band variations are regularly observed, whereby variable hard photons lag behind soft photons with a delay of order 1 percent of the variability timescale (hereafter "hard lags", e.g. Nowak et al. 1999; Grinberg et al. 2014). Various mechanisms have been proposed to explain the observed X-ray spectral-timing behaviour of BHXRBs (Poutanen & Fabian 1999; Misra 2000), with models of inward propagation of mass accretion rate fluctuations currently offering the most compelling physical explanation (Lyubarskii 1997; Kotov et al. 2001; Arévalo & Uttley 2006; Ingram & van der Klis 2013; Mushtukov et al. 2018; Mahmoud & Done 2018a,b; Bollimpalli et al. 2020).

However, an important additional component of high mass X-ray binary systems like Cyg X-1 is the stellar wind from the companion, early type, supergiant star. Evidence for the presence of a stellar wind was soon found in Cyg X-1 (e.g., Li & Clark 1974; Remillard & Canizares 1984; Bałucińska-Church et al. 2000; Miller et al. 2005; Poutanen et al. 2008; Hanke et al. 2009; Grinberg et al. 2015; Miškovičová et al. 2016). The strong line-driven wind presents an inhomogeneous structure, with clumps characterized by highly dense regions (Owocki & Rybicki 1984; Owocki et al. 1988; Feldmeier 1995). When a clump intercepts our line of sight to the X-ray source, the X-ray emission is partially absorbed by the wind material leading to a dipping event (sudden drop of the X-ray flux). Such events occur more frequently and are more intense at superior conjunction, i.e. when the compact object lies behind the donor star (at orbital phase $\phi_{\rm orb} = 0$ and our line of sight probes regions of the stellar wind closer to the surface of the companion, e.g. Bałucińska-Church et al. 2000; Grinberg et al. 2015; Miškovičová et al. 2016).

It is reasonable to expect that wind absorption does not only affect the observed spectrum, but also the observed X-ray variability properties of the source (Grinberg et al. 2015, 2020). For example, motions of wind clumps through our line of sight to the X-ray source are expected to produce X-ray spectral-timing signatures on the relevant timescales (El Mellah et al. 2020). Given current estimates of the size of the clumps, such timescales can be of the order of minutes or shorter (Grinberg et al. 2017; Hirsch et al. 2019). In addition, the wind is found to be affected by the radiation field around the BH, resulting in stronger absorption during the hard state than during the soft state (Boroson & Vrtilek 2010; Nowak et al. 2011). Given the strong flux variability characterising the hard state of BHXRBs (Muñoz-Darias et al. 2011; Heil et al. 2012), additional wind variability due to changes in the irradiating flux might be expected (Nicastro et al. 1999; Krongold et al. 2007; Silva et al. 2016).

All this suggests that the observed X-ray spectral-timing characteristics of Cyg X-1 can be significantly influenced by the stellar wind, thus affecting any study aimed at constraining the intrinsic properties of the X-ray source. On the other hand, the X-ray spectral-timing signatures characteristics of the most wind-absorbed phases can be a powerful tool to determine the physical properties of the wind (e.g. Grinberg et al. 2015; Silva et al. 2016; De Marco et al. 2020; El Mellah et al. 2020).

Cyg X-1 has been recently the target of an unprecedented long multiwavelength monitoring campaign, the "Cyg X-1 Hard state Observations of a Complete Binary Orbit in X-rays" (CHOCBOX) campaign, with XMM-Newton as the primary instrument. The XMM-Newton monitoring consists of four observations of the source in its hard state, for a total exposure of about $\sim$ 572 ks and covering about one and a half orbital periods (7.22 d). In this paper, we study this long dataset, focusing on determining how the variability of the stellar wind influences the X-ray spectral-timing properties of the source.

2 DATA REDUCTION

For the spectral-timing measurements, which are optimised for high count rates, we consider only the EPIC-pn data. The four observations analysed were carried out between 2016 May 27 and June 2, with a total exposure of $\sim$ 572 ks (before data screening). The analysed data are acquired in Timing mode. The log of the observations is reported in Tab.1. Hereafter, we will refer to each observation using the last three digits of their ObsID (as specified in Tab.1).

The data reduction has been carried out using the XMM-Newton Science Analysis System (SAS) software (version 16.9.0), following standard procedures. In order to identify and filter out time intervals affected by high particle background, we extracted light curves with a time resolution of 1 s in the energy range 10–15 keV (where the instrument response drops). We checked the light curves to identify background flares, but none was found.

The analysed observations are affected by telemetry drop-outs, i.e. periods of high count rate producing buffer overflow, during which photons are not collected. These periods result in gaps in the data, which are accounted for in the selection of Good Time Intervals, GTIs, using the SAS task `tabgtigen`. The resulting GTIs are very short during all observations, with an average length of $\sim$ 10 s.

We extracted source counts in the range RAWX:30–46. Using the SAS task `epatplot`, we checked for the presence of pile-up. We found that the data are affected by some fraction of pile-up, thus we mitigated it by excluding the central (RAWX:36–39) pixels. Since the observations are in Timing mode, it is not possible to select a source-free region for extraction of background events, while subtracting the background from the outer columns (RAWX intercepting the tails of the PSF) may modify the source spectrum (Ng et al. 2010). However, the source is very bright (with a 0.5–10 keV average count rate of $\sim$ 220 counts/s), thus the effects of background are expected to be negligible (e.g. Ng et al. 2010). Finally, we notice that the most absorbed periods, thus potentially more affected by the background, are excluded in our spectral analysis (Sect. 4), while the background is not expected to contribute to the rapid X-ray variability of BHXRBs (e.g. Uttley et al. 2011; De Marco et al. 2017). Therefore, we decided not to subtract the background.

Ancillary response files (ARF) and redistribution matrix files (RMF) were extracted using the SAS tools `arfgen` and `rmfgen`. We generated an ARF for the full region (RAWX:30–46) and a second ARF for the excluded region (RAWX:36–39). The ARF of our extraction region was obtained by subtracting the latter from the former using the command `addarf` (e.g. Wilkinson & Uttley 2009). We used calibration files (CCF) as of June 2019. The spectra were re-binned to have a minimum of 20 counts in each energy bin. For

Table 1. Log of the XMM-Newton EPIC-pn observations analysed. Effective exposures after regular data screening (Total exposure) and after the additional selection of time intervals not affected by wind absorption (NWA exposure) are reported. The orbital phase $\phi_{\rm orb}$ is computed using the ephemeris reported in Gies et al. (2008). The last three digits of the ObsID used throughout the test to identify each observation are marked in boldface.

ObsID	Date (yyyy–mm–dd)	Total exposure (ks)	NWA exposure (ks)	$\phi_{\rm orb}$
0745250**201**	2016–05–27	92.9	30.9	0.82–0.06
0745250**501**	2016–05–29	83.1	79.8	0.17–0.46
0745250**601**	2016–05–31	76.7	74.8	0.53–0.79
0745250**701**	2016–06–02	84.6	44.9	0.89–0.11

the spectral fits (Sect. 4) we used Xspec v12.10.1 (Arnaud 1996), while codes for the spectral-timing analysis (Sects. 3 and 4) were implemented using Python 3.6.

2.1 Selection of events not affected by wind absorption

Depending on the orbital phase of the compact object the X-ray emission will be more or less absorbed by the stellar wind. As a consequence of the orbital modulation of the intervening absorbing column, light curves show recurrent dips of variable intensity. Due to the spectral dependence of the opacity of the wind, the soft X-ray band is the most affected.

Fig. 1 shows the EPIC pn light curves of the source extracted (with a time bin of 10 s) in the two energy bands: 0.5–1.5 keV and 3–10 keV. During the monitoring, two consecutive passages at superior conjunction (occurring during observations 201 and 701) are observed. These are marked by red vertical lines in Fig. 1. The 0.5–1.5 keV light curve (Fig. 1, top panel) shows several dips, in particular around superior conjunction. Such dips are less intense in the 3–10 keV energy band (Fig. 1, middle panel), resulting in a net increase of the spectral hardness (defined as the ratio between count rates in the 3–10 keV and 0.5–1.5 keV energy bands; Fig. 1, bottom panel). We note that, though clustering around superior conjunction (at the beginning and at the end of the monitoring), dips are sparsely present throughout the entire campaign.

We followed the method proposed in Nowak et al. (2011) and Hirsch et al. (2019) to select time intervals not affected by absorption. The method consists in constructing a colour-colour diagram which shows the time-resolved spectral behaviour of the source. The diagram displays ratios between a soft and an intermediate band (soft colour) and between an intermediate and a hard band (hard colour). The position of the source in the colour-colour diagram depends on the amount of absorption along the line of sight (Grinberg et al. 2020).

In order to build the colour-colour diagram, we used light curves with a time bin of 10 s so as to uncover also very short dips. We considered the three energy bands 0.5–1.5 keV, 1.5–3 keV, and 3–10 keV (hereafter soft, intermediate, and hard). The resulting colour-colour diagram for each XMM-Newton observation is shown in Fig. 2.

Following Hirsch et al. (2019), time intervals characterised by high values of both hard and soft colours (upper right corner of the colour-colour diagram) are the least affected by wind absorption. In order to extract a dataset relatively free from wind absorption, we thus selected events from that region of the diagram by defining a threshold for the hard and soft colours. We selected all the 10 s–long data segments with a hard colour $\geqslant 0.95$ and a soft colour $\geqslant 0.7$. We consider the simple model adopted in Hirsch et al. (2019), which comprises a power law with spectral index 1.7 partially covered by a neutral absorber (representing the clumpy wind), modified by Galactic absorption (`tbnew` $\times$ `tbpcf` $\times$ `powerlaw` in Xspec, with Galactic $N_{\rm H} = 0.7 \times 10^{22}\,{\rm cm}^{-2}$; Basak et al. 2017; HI4PI Collaboration et al. 2016; and assuming abundances from Wilms et al. 2000[1]). For this model, we find that if the partial covering factor is kept constant and only the wind column density varies, the theoretical curve that best samples the range of hard and soft colours covered by the data corresponds to a covering factor of ~ 0.9. For such a value of the covering factor, the chosen threshold of hard and soft colours selects data characterised by a wind column density $N_{\rm H,w} \lesssim 1.08 \times 10^{22}\,{\rm cm}^{-2}$. The final datasets resulting from the described filtering process will be hereafter referred to as "NWA" (standing for "no wind absorption") as opposed to "Total", which will be used to refer to the datasets unfiltered from wind absorption. It is worth noting that the inferred theoretical curve describing the colour-colour tracks and the corresponding physical parameters represent just an approximation. Indeed, the curve does not accurately reproduce the observed tracks (Appendix A). As discussed in Grinberg et al. (2020), this highlights the need for more complex absorption models in order to properly describe these tracks. While this is beyond the scope of this paper, this issue will be addressed in a follow up paper.

It is worth noting that our filtering choices, together with the use of a 10 s time bin for the light curves employed to build the colour-colour diagram, ensure a good filtering of strong wind absorption events of duration $\geqslant 10$ s. Nonetheless, residual absorption might still be present. Wind clumps characterised by lower $N_{\rm H,w}$ and/or lower covering factor, and moving faster across the line of sight (thus producing shorter dips) would be the major contributors to this residual absorption.

3 POWER SPECTRA

In order to study the effects of the stellar wind on the X-ray variability of the source we first extracted the PSD of the NWA and Total datasets of each observation. The PSD were extracted in the soft, intermediate and hard energy bands defined in Sect. 2.1. To this aim we used light curves with a time resolution of 6 ms. The light curves were split into segments, containing 1666 data points each (which correspond to a length of 9.996 s). This allows us to sample the range of temporal frequencies $\nu \sim 0.1$–83 Hz (corresponding to variability timescales between ~ 0.01–10 s). The chosen segment length is the result of a trade-off between obtaining a sufficiently broad frequency coverage while retaining a high number of GTIs. We calculated the PSD of each segment and then averaged over all segments. We adopted the fractional rms normalization (Belloni & Hasinger 1990; Miyamoto et al. 1991). We did so for each observation separately, in order to study the evolution of the wind-modulated variability as a function of the orbital phase. We estimated the Poisson noise contribution by fitting the PSD with a constant at frequencies > 25 Hz. We corrected the PSD for Poisson noise by subtracting this contribution. The PSD was geometrically rebinned, using a rebinning factor of $\nu_{i+1} = 1.2\,\nu_i$.

In Fig. 3, we compare the PSDs obtained from the NWA and Total datasets. The PSDs are shown separately for each observation

[1] https://pulsar.sternwarte.uni-erlangen.de/wilms/research/tbabs/

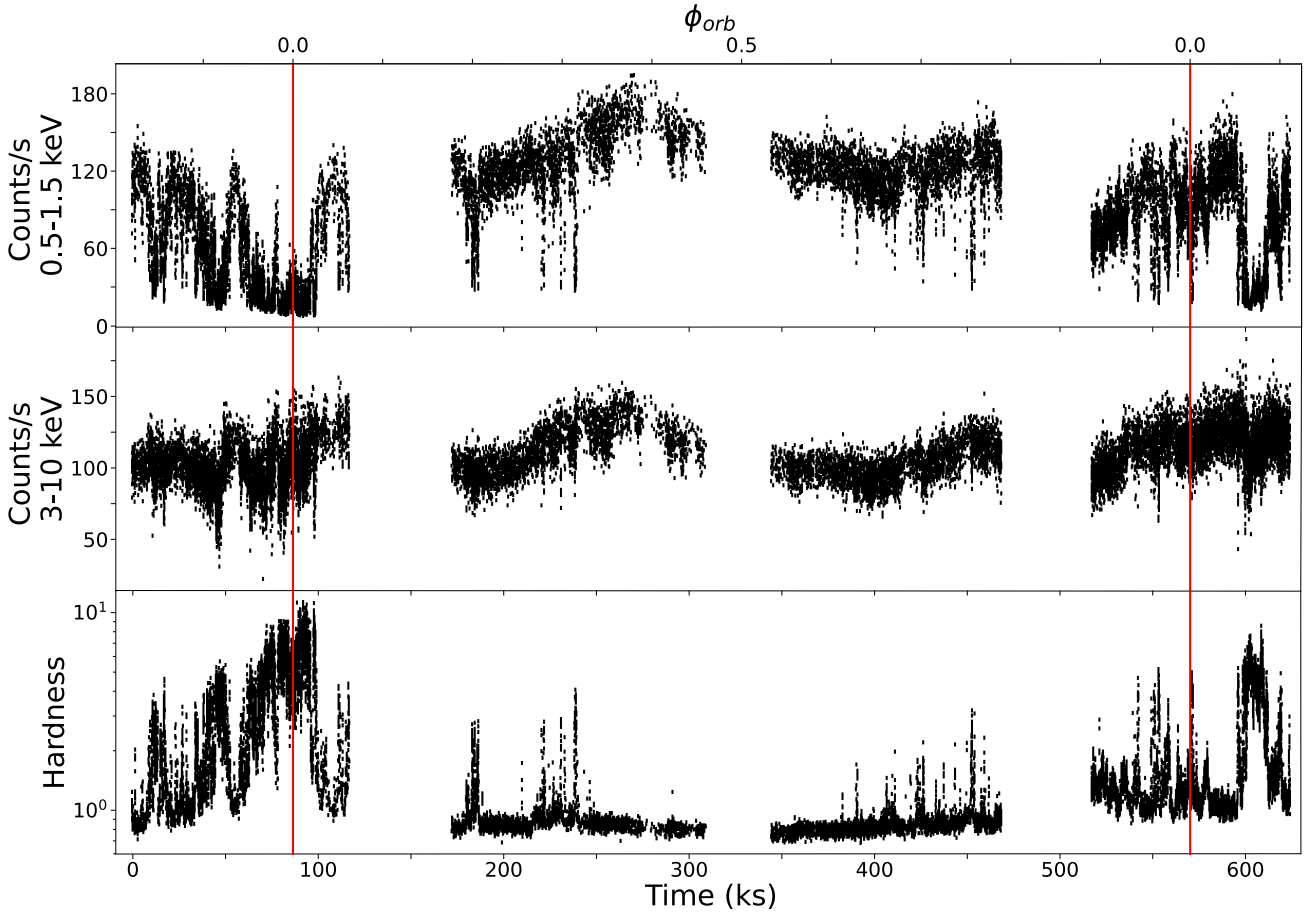

Figure 1. XMM-Newton EPIC-pn light curves of the four analysed observations of Cyg X-1 (i.e. observations 201, 501, 601, and 701, each separated by the gaps in the light curve). The reference starting time of the monitoring is 57535.0 MJD. The upper panel reports the 0.5–1.5 keV light curve. The middle panel reports the 3–10 keV light curve. The bottom panel reports the ratio between count rates in the 3–10 keV and 0.5–1.5 keV energy bands. The red lines indicate the two consecutive passages at superior conjunctions ($\phi_{\rm orb} = 0$) occurring during the XMM-Newton monitoring.

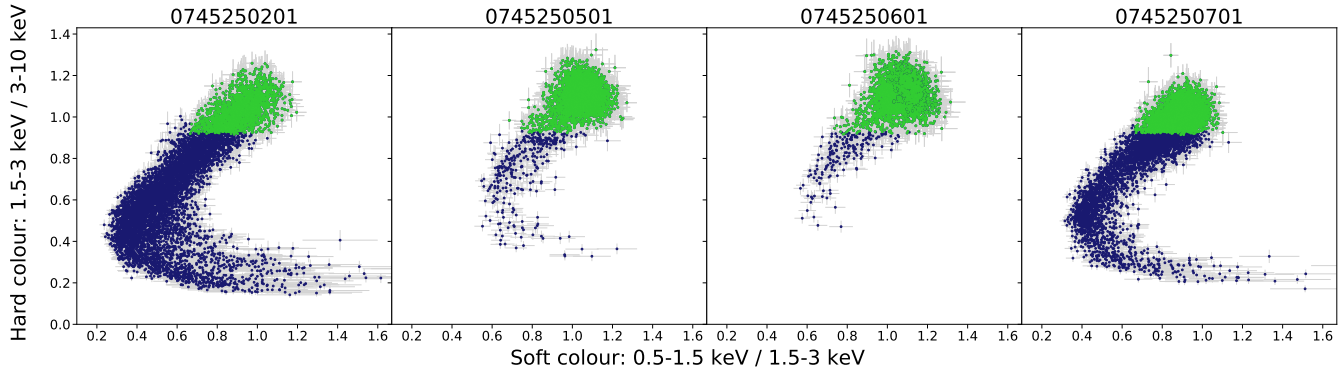

Figure 2. The colour-colour diagram of each XMM-Newton observation, showing hard and soft colours calculated for soft (0.5–1.5 keV), intermediate (1.5–3 keV) and hard bands (3–10 keV). Each point in the plot corresponds to a 10 s–long data segment. Time intervals in green are those characterised by values of hard colour $\geqslant 0.95$ and soft colour $\geqslant 0.7$, thus representing our selection of NWA datasets, the least affected by wind absorption.

and for the soft, intermediate, and hard energy bands. We observe that the wind contributes significantly to the short-timescale X-ray variability. The main effect of the wind is that of smoothing out the typical double-hump shape of the PSD of Cyg X-1 in the hard state (e.g. Pottschmidt et al. 2003; Axelsson & Done 2018; Mahmoud & Done 2018a,b). This shape is recovered when considering the NWA datasets and when the source is not at superior conjuction (thus it is less affected by wind absorption). More specifically, wind absorption tends to reduce (by up to a factor of ~ 2) the fractional variability at high frequencies ($\gtrsim 1$ Hz), and to increase it at low frequencies ($\lesssim 1$ Hz), as most clearly seen in observation 201.

However, given the limited bandpass, the effects of the wind at low frequencies are more difficult to constrain.

Notably, the PSD of observation 701 remains quite smooth also after filtering out wind-absorbed segments. We verified that this is due to residual wind absorption. Indeed, when choosing a tighter threshold of hard and soft colours for the selection of the NWA dataset (Sect. 2.1), the double-hump shape appears (Appendix B). This different selection also allows for additional low-frequency variability due to the wind in the Total dataset to be clearly observed in this observation as well. The need for a different threshold suggests that the average properties of the wind may be different between consecutive passages at superior conjunction (as also indicated by the different extension of the colour-colour track towards low values of soft colours and the spread around the main track[2], during observations 201 and 701, Fig. 2). Nevertheless, a tighter threshold for the selection of NWA events in observation 701 severely reduces the amount of usable exposure (thus decreasing the signal-to-noise of spectral-timing measurements). For this reason, and for consistency with the other observations, we decided to use the same selection criteria as for the other observations (Sect. 2.1).

Finally, it is worth noting that the effects of the wind on the PSD of the source are not limited to the soft (and more absorbed) energy bands, but can be observed up to the highest sampled energies (i.e. E = 3–10 keV), suggesting rather high column densities.

4 CROSS SPECTRAL ANALYSIS

Cross-spectral analysis informs us about the amount of correlated variability and the causal relationship between different spectral components (e.g. Nowak et al. 1999; Uttley et al. 2014). It is well-known that in the hard state of BHXRBs the primary Comptonisation component and the disc vary in a linearly correlated way, showing high levels of coherence on a broad range of timescales (e.g. Wilkinson & Uttley 2009). In addition, the disc is observed to lead the variations of the Comptonisation component on the long timescales (> 1 s, Uttley et al. 2011), while, for some sources, it is observed to respond to hard X-ray variability on the shortest sampled timescales (< 1 s) (Uttley et al. 2011; De Marco et al. 2015; Kara et al. 2019; De Marco et al. 2021). The former behaviour is usually interpreted in terms of inward propagation of mass accretion rate fluctuations in a spectrally inhomogeneous medium (Lyubarskii 1997; Kotov et al. 2001; Arévalo & Uttley 2006; Ingram & van der Klis 2013; Mushtukov et al. 2018; Bollimpalli et al. 2020), while the latter is ascribed to the thermal response of the disc to variable hard X-ray irradiation (thermal reverberation, e.g. Uttley et al. 2011; De Marco et al. 2015; De Marco & Ponti 2016; De Marco et al. 2017; Kara et al. 2019; Wang et al. 2020; De Marco et al. 2021). In this section, we analyse the X-ray cross-spectral timing properties of Cyg X-1 in order to study the correlations and causal relationship between the disc and the primary Comptonisation components, and estimate the effects of the wind on such properties.

We first identified the energy bands where the disc and the Comptonisation component dominate by fitting the time-averaged spectra of the source. In order to minimise the effects of the wind on the primary X-ray continuum, the spectra were extracted considering only the NWA dataset. The time-averaged spectra of all observations were fit jointly. We discarded data below 0.7 keV in order to avoid distortions due to electronic noise in Timing mode (calibration file: XMM-CCF-REL-265, Guainazzi, Haberl and Saxton 2010)[3].

The model used for the fit is `TBnew × [diskbb + nthComp + relxillCp]` in Xspec. It includes a multicolour disc component, `diskbb`, (Mitsuda et al. 1984), and the soft excess, well modelled by a soft Comptonisation component, `nthComp` (Zdziarski et al. 1996; Życki et al. 1999). Even though difficult to physically interpret, this component is necessary to obtain a reasonable fit (e.g. Zdziarski & Gierliński 2004; Basak et al. 2017). The `relxillCp` (Dauser et al. 2014; García et al. 2015) component has been used to model the hard Comptonisation component and its associated reflection spectrum from the inner disc. Among the different spectra, we tied the inclination and the column density of the ISM to be the same for each observation, whereas for every single spectrum, we tied the seed photon temperature to the inner disc temperature and we fixed the high-energy cut-off of the hard Comptonisation component at 100 keV (Basak et al. 2017). The column density of the ISM was left free to vary in order to account for possible residual wind absorption. Indeed, we found $N_H \sim 0.9 \times 10^{22}$ cm^{-2}, slightly higher than the value measured in Galactic neutral atomic Hydrogen column density surveys (i.e. 0.7×10^{22} cm^{-2}, HI4PI Collaboration et al. 2016). We observe significant residuals at energies between 1.5 and 2.5 keV, i.e. around the absorption edges of the detector, likely associated with incorrect calibration. Indeed, after ignoring this energy range the fit significantly improves, with a χ^2/dof = 11582/8268. We found an inner disc temperature in the range $kT_{in} \sim$ 0.17–0.2 keV and a spectral index for the hard Comptonisation component $\Gamma_H \sim$ 1.3–1.4 (see Table C1).

In Fig. 4 we show the spectrum, the best-fit model and their ratio for each observation. We see that the disc dominates below ∼ 1 keV and that the 2–10 keV energy band is dominated by the hard X-ray primary emission. Thus we decided to use the energy bands 0.3–1 keV and 2–10 keV for the computation of cross spectra. We extracted light curves in these two energy bands, using the same sampling parameters (time bin and segments length) as used for the computation of the PSDs (Sect. 3). For each light curve segment, we computed the cross-spectrum, then we averaged over the different cross spectra. Following Ingram (2019), we rebinned the cross spectra in order to have a minimum number of 500 points per frequency bin to obtain good S/N, so to avoid the complexities of defining the Poisson noise contribution. This procedure was repeated separately for the NWA and Total datasets of each observation. We used the average cross spectra to compute time lags and coherence as detailed in Sects. 4.1 and 4.2.

4.1 Coherence as a function of frequency

The coherence measures the degree of linear correlation between two light curves as a function of Fourier frequency (e.g. Vaughan & Nowak 1997; Nowak et al. 1999; Uttley et al. 2014). Fig. 5 shows the intrinsic coherence (computed using equation 8 of Vaughan & Nowak 1997) for the Total and the NWA datasets, between the 0.3–1 keV and 2–10 keV light curves.

Above ∼ 10 Hz the intrinsic coherence has large uncertainties because of a significant contribution from uncorrelated Poisson noise. Therefore, we decided to limit our analysis to the frequencies less affected by Poisson noise (i.e. 0.1–10 Hz).

[2] We note that in general, spectral hardening and/or softening of the source may also produce such changes in the colour-colour tracks (e.g. see figure 2 of Grinberg et al. 2020). However, our best-fit models do not show significant difference in spectral slope between these two observations, Table C1.

[3] https://www.cosmos.esa.int/web/xmm-newton/ccf-release-notes

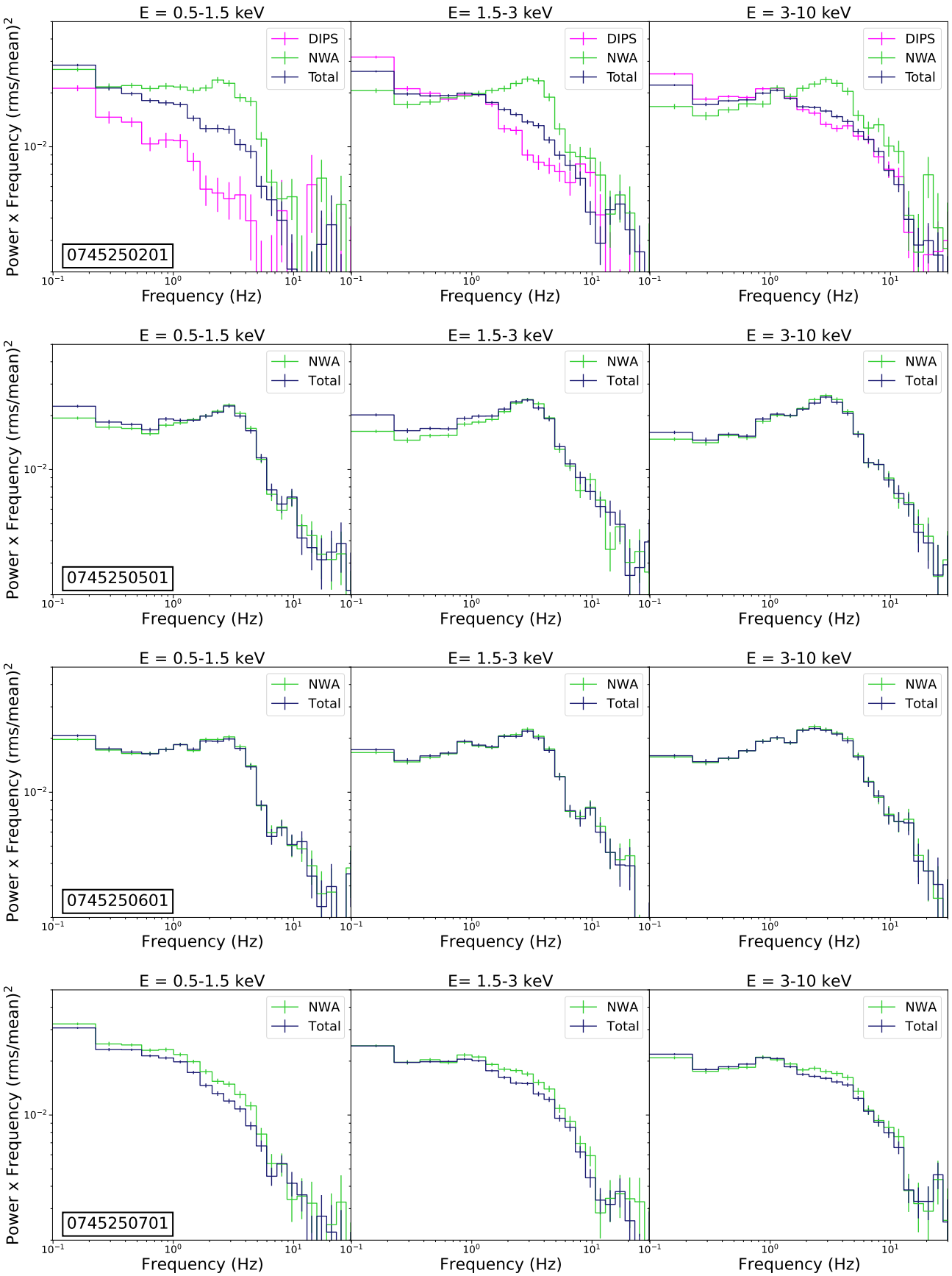

Figure 3. PSD for the Total (blue), the NWA (green) datasets of each observation (from top to bottom) in the soft (0.5–1.5 keV), intermediate (1.5–3 keV) and hard (3–10 keV) energy bands (from left to right). For observation 201 we also show the PSD obtained from selection of the wind-dominated (characterized by a hard colour $\leqslant 0.8$, Sect. 4.3) "DIPS" dataset (in magenta).